THE JOURNAL OF PHYSICAL CHEMISTRY B
A JOURNAL OF THE AMERICAN CHEMICAL SOCIETY

pubs.acs.org/JPCB Article

Charge Distribution Patterns of IA_3 Impact Conformational Expansion and Hydration Diffusivity of the Disordered Ensemble

Katie M. Dunleavy, Tianyan Li, Eugene Milshteyn, Afnan M. Jaufer, Shamon A. Walker, and Gail E. Fanucci*

Cite This: *J. Phys. Chem. B* 2023, 127, 9734−9746 **Read Online**

ACCESS | Metrics & More | Article Recommendations | Supporting Information

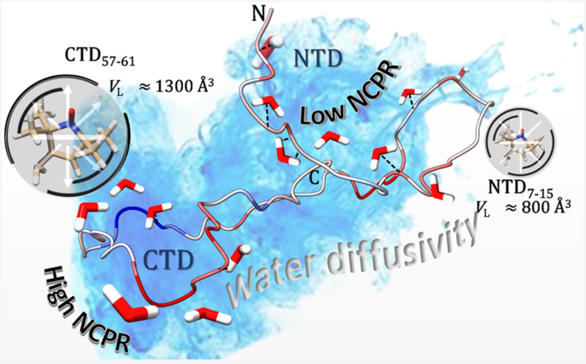

ABSTRACT: IA_3 is a 68 amino acid natural peptide/protein inhibitor of yeast aspartic proteinase A (YPRA) that is intrinsically disordered in solution with induced N-terminal helicity when in the protein complex with YPRA. Based on the intrinsically disordered protein (IDP) parameters of fractional net charge (*FNC*), net charge density per residue (*NCPR*), and charge patterning (κ), the two domains of IA_3 are defined to occupy different domains within conformationally based subclasses of IDPs, thus making IA_3 a bimodal domain IDP. Site-directed spin labeling (SDSL) electron paramagnetic resonance (EPR) spectroscopy and low-field Overhauser dynamic nuclear polarization (ODNP) spectroscopy results show that these two domains possess different degrees of compaction and hydration diffusivity behavior. This work suggests that SDSL EPR line shapes, analyzed in terms of their local tumbling volume (V_L), provide insights into the compaction of the unstructured IDP ensemble in solution and that protein sequence and net charge distribution patterns within a conformational subclass can impact bound water hydration dynamics, thus possibly offering an alternative thermodynamic property that can encode conformational binding and behavior of IDPs and liquid−liquid phase separations.

■ INTRODUCTION

Intrinsically disordered proteins (IDPs) and proteins containing intrinsically disordered regions (IDRs) lack a well-defined secondary/tertiary structure making up a class of proteins not defined by the standard structure-to-function paradigm.[1−7] Proteins containing disorder in 30 or more residues are defined as IDPs and IDRs with global or local disorder, respectively.[3,8−11] More than 15% of all eukaryotic proteins are determined to contain intrinsic disorder, signifying an important benefit of disorder.[9,12] Proteins containing local or global disorder under physiological conditions can benefit a cellular system by allowing for more dynamic linking regions, ease in finding a binding target due to overall flexibility, multiple binding targets, and conformational sampling.[3,9,10,12] Cellular signaling pathways and cellular regulation depend on these advantages, making IDPs highly associated with these processes.[3,13,14] Key amino acid residues are known to promote disorder through charged and structure-perturbing side chains, as opposed to hydrophobic and aromatic residues that induce the protein structure.[1,2,4−7,11,15−20] Due to the depletion of structure-promoting residues and an increase in overall charged residues, IDPs adopt low mean hydrophobicity and overall high net charge.[2,9,11]

IA_3 is a 68 amino acid inhibitor of yeast aspartic proteinase A (YPRA).[21] In general, proteases play important roles in many physiological as well as pathological processes. As such, there is interest in the continued discovery, modification, and development of novel protein-based protease inhibitors for use as versatile tools in the fields of medicine, agriculture, and biotechnology.[22−24] IA_3 is intrinsically disordered in solution (a.k.a. an IDP) and adopts an N-terminal domain (NTD) α-helix with an unresolved C-terminal domain (CTD) in the crystallographic complex when bound to YPRA (Figure 1A).[21] Previous studies demonstrate that the NTD 32 residues of IA_3 are responsible for its inhibitory activity.[25−27] In the absence of YPRA, the helical structure throughout both the NTD and CTD of IA_3 can be induced by 2,2,2-trifluoroethanol (TFE).[28] The TFE-induced helical transitions in *Saccharomyces cerevisiae* IA_3 have been studied using circular dichroism (CD), 2D ^1H ^{15}N nuclear magnetic resonance (NMR), laser temperature-jump fluorescence and fluorescence resonance energy transfer (FRET), and site-directed spin labeling (SDSL) electron paramagnetic resonance (EPR) spectroscopies.[28−35] The CTD

Received: September 13, 2023
Revised: October 27, 2023
Accepted: October 27, 2023
Published: November 8, 2023

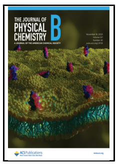

https://doi.org/10.1021/acs.jpcb.3c06170

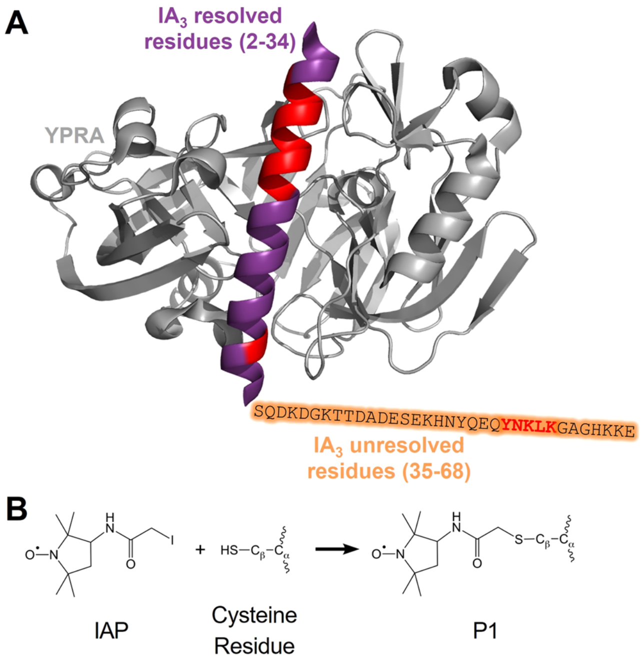

Figure 1. (A) Ribbon diagram of IA$_3$ when bound to YPRA (PDB: 1DPJ)[21] with the helical N-terminal domain (NTD) shown in purple and disordered C-terminal domain (CTD) not resolved in the complex represented as an extended sequence highlighted in orange. (A) P1-labeled cysteine variant sites are rendered in red (amino acid sequence given in Figure S1). (B) Reaction scheme of IAP (3-(2-iodoacetamido)-PROXYL) attachment to a cysteine residue resulting in P1-labeled side chain.

of *S. cerevisiae* IA$_3$ does adopt a helical structure in TFE, albeit to a lesser degree than the NTD.[28,29,32,33,36]

SDSL is a sensitive method to interrogate the local microenvironment via probing conformational dynamics and changes in biomolecular and macromolecular systems through analysis of and changes therein of the nitroxide EPR line shape, which is sensitive to molecular motions on the ns time scale.[37−41] Although commonly utilized for structured soluble and membrane proteins,[42,43] SDSL has found application to the study of IDPs.[32−35,44−49]

We have previously studied the TFE-induced helical transition in IA$_3$ with SDSL and CD spectroscopies.[32−35] Results, consistent with earlier circular dichroism (CD) spectroscopy[28] and NMR investigations,[29] showed that the helical transition of the CTD was less cooperative than the NTD and that the CTD does not undergo the same extent of TFE-induced helical transition. We also demonstrated with SDSL EPR and CD that the degree of the TFE-induced helical transition of the NTD is mitigated by amino acid substitution that disrupts the hydrogen-bonding network on the hydrophilic face of the helix[36] and that the incorporation of the nitroxide spin label, 3-(2-Iodoacetimido)-PROXYL (IAP, termed P1 when chemically attached to a cysteine side chain) (Figure 1B), generated constructs that possess greater than (S9P1,Q13P1), less than (V8P1, E10P1, I11P1, S15P1), or equivalent to (K7P1, F12P1, S14P1) the TFE-induced helical propensity as wildtype (WT) IA$_3$.[33] CTD P1 variants Y57P1, N58P1, K59P1, L60P1, and K61P1 have similar TFE-induced helical propensity as WT.[33,50]

Having a series of spin-labeled constructs with known WT behavior allows for continued investigations of differences in the local properties and behavior of the two domains of IA$_3$. Local hydration dynamics within 5−10 Å of a nitroxide radical spin probe can be probed with low-field ODNP. This method combines ∼9.5−9.8 GHz X-band continuous-wave EPR (CW-EPR) and ∼14.6−14.8 MHz nuclear magnetic resonance (NMR) techniques to amplify the ^{1}H NMR signal of local water molecules.[51−54] At 0.35 T, the Overhauser effect transfers polarization from the electron spin to adjacent water molecules due to electron-^{1}H dipolar coupling via cross-relaxation, enhancing the ^{1}H NMR signal through saturation of the electron spin, giving rise to local water diffusivity relative to the proximity of the electron spin probe.[51,55,56] The time needed for water to diffuse through the 5−10 Å distance surrounding the spin label is defined as the translational diffusion correlation time (τ_c). Through measurements of the ^{1}H NMR signal enhancement via ODNP and T_1 relaxation time changes due to the presence of the spin label, the contributions from local electron-^{1}H cross-relaxation (k_σ) can be separated from local waters undergoing self-relaxation (k_ρ).[57] The coupling factor (ξ), a ratio of k_σ and k_ρ, is a parameter that describes water diffusivity and has been separated into different environments, such as bulk-like ($\xi > 0.153$), surface ($0.076 < \xi \leq 0.153$), intermediate ($0.043 < \xi \leq 0.076$), or buried ($\xi \leq 0.043$) (Figure 2), based on experimental results of Han and co-workers for known spin-label locations in macromolecules encompassing proteins, polymers, and lipid dispersions.[52] The experimentally determined value of ξ, using the force-free hard sphere (FFHS) model of translational diffusion[58] to calculate the spectral density function for how the overall time scale of the dynamics modulates the dipolar interaction between the spin label and water, can be converted into a correlation time τ_c.

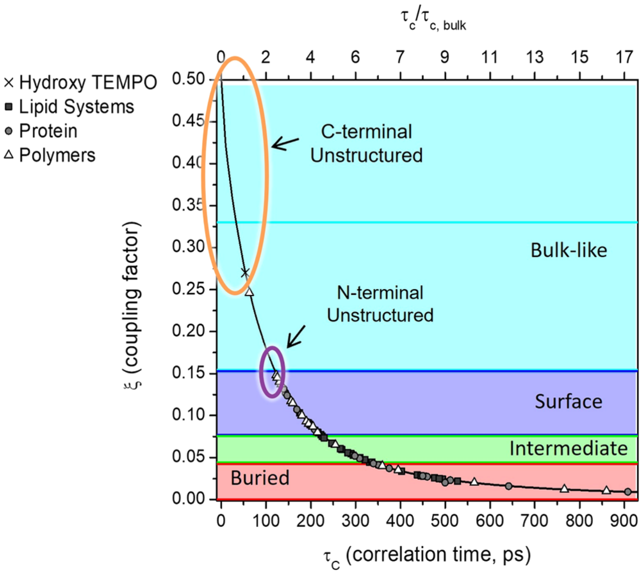

Figure 2. Plot of collective literature-based ξ values and their modeled relationship to τ_c and $\tau_c/\tau_{c,bulk}$ for spin label hydroxyTEMPO (x), lipid systems (solid squares), proteins (gray circles), and polymers (open triangles).[51−53,60−64] Results discussed within for IA$_3$ NTD (purple oval) and CTD (orange oval) sites are graphically depicted to show that anomalously fast hydration dynamics was observed for CTD sites, with the NTD region giving interfacial hydration dynamics. Figure modeled after those shown in ref 51 by Han and co-workers.

https://doi.org/10.1021/acs.jpcb.3c06170
J. Phys. Chem. B 2023, 127, 9734−9746

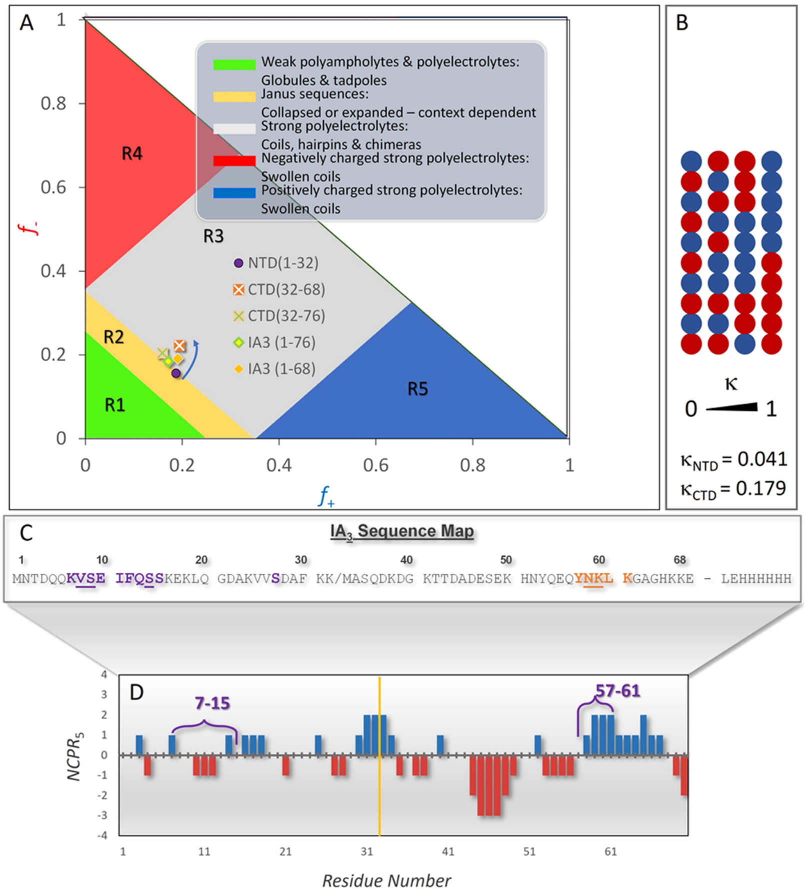

Figure 3. Sequence analysis of *S. cerevisiae* IA_3 NTD and CTD within (A) subclass in Pappu plot, (B) κ values, (C) amino acid sequence, where the forward slash after residue K32 marks the end of the NTD as defined by the sequence that gives optimal inhibition of YPRA, and with NTD and CTD sites studied by SDSL EPR in purple and orange, respectively.[27] Underlined residues are those P1-labeled sites studied via low-field ODNP. (D) FCR/NCPR/κ analysis as a function of sequence with a blob size of 5 using CIDER. Sections A and B are modeled after refs 2 and 7.

The solid line in Figure 2 is a graphical representation of this equation (eq S3), which is used to show relationships between local water diffusivity properties and the measured value of ξ. The ratio of ξ/ξ_{bulk} (or $\tau_c/\tau_{c,bulk}$) can be used as a comparative parameter to describe the effective retardation in hydration diffusivity relative to bulk water.[52] These experimentally determined parameters can further differentiate fast diffusing water (DW) on the picosecond time scale (k_σ) and slower diffusing or "bound" water (BW—waters that have rotational correlation times dictated by the macromolecule) on the millisecond–nanosecond time scale (k_{low}).[55,57,59]

Here, we extend our studies of IA_3 via SDSL EPR and low-field ODNP by characterizing the two domains (NTD and CTD) of IA_3 as separate conformational subclasses of IDPs. Our CW-EPR and ODNP results reveal differences in the average local tumbling volume (i.e., compaction) and the hydration dynamics of the two disparate domains for the intrinsically disordered state of this IDP. This work adds to the growing interest in understanding how structural and dynamic properties of IDPs are controlled by charge and sequence patterning.[1,2,4,6,7,17−20,65] A deeper comprehension of these effects can impact our fundamental understanding of physiological and pathological processes and inform the rational design of IDPs as bioinspired materials with biotechnological applications.

■ MATERIALS AND METHODS

Materials. BL21-DE3-pLysS and XL-1 blue *Escherichia coli* cells used in protein overexpression and DNA amplification were purchased from Invitrogen (Carlsbad, CA). pET-22b+ and 3-(2-Iodoacetamido)-PROXYL spin label were purchased from Millipore Sigma (Burlington, MA). Primers for cysteine residue site-directed mutagenesis were purchased from Integrated DNA Technologies (Coralville, IA). Restriction enzymes (*Xho*I, *Nde*I), T4 ligase, Phusion HF DNA polymerase, and DpnI for cloning and mutagenesis were purchased from New England Biolabs, (Ipswich, MA). A HiTrap Chelating HP and HiTrap 26/10 Desalting columns were purchased from GE Healthcare Life Sciences (Chicago, IL). 16.5% Tris-Tricine SDS-PAGE gels were purchased from Bio-Rad Laboratories (Hercules, CA). The 0.60 i.d. x 0.84 o.d. quartz capillary tubes for CW-EPR and ODNP were purchased from the Fiber Optic Center (New Bradford, MA). Cha-Seal was purchased from Kimble Chase Life Science (Rockwood, TN). Unless otherwise noted, all other products and reagents were purchased from Fisher Scientific (Pittsburgh, PA).

Protein Expression and Purification of IA_3 Mutants. The *E. coli* codon-optimized gene of IA_3 (UniProt P01094) was cloned into a pET-22b+ vector (Invitrogen) containing a C-terminal 6× His-tag, adding the sequence LEHHHHHH to the C-terminus (Figures 3 and S1).[32] Constructs K7C, V8C, S9C, E10C, I11C, F12C, Q13C, S14C, S15C, S27C, Y57C, N58C, K59C, L60C, and K61C were generated as described previously.[33] Wildtype and cysteine-substituted IA_3 protein variants were purified using nickel affinity chromatography and eluted in 50 mM sodium phosphate, 300 mM sodium chloride, and pH 4.0 as described previously.[32] To chelate residual nickel and to ensure cysteine reduction, ethylenediaminetetraacetic acid (EDTA) and dithiothreitol (DTT) were added to purified constructs to concentrations of 100 and 0.1 mM, respectively. Protein purity was assessed by using a 16.5% mini-PROTEAN Tris-Tricine SDS-PAGE gel.

Spin Labeling. Purified IA_3 fractions were pooled, concentrated, and buffer exchanged into 50 mM sodium phosphate and 300 mM sodium chloride, pH 7.4, using a HiTrap 26/10 desalting column to remove residual nickel, EDTA, and DTT prior to spin labeling. Upon buffer exchange, cysteine-substituted constructs were immediately reacted with 5−10× molar excess IAP spin label dissolved in 50−100 μL of 100% ethanol for 12 h at 4 °C, in the dark. The labeling scheme is shown in Figure 1B. Excess spin label was removed through repeated buffer exchange, as described above. If necessary, spin-labeled protein samples were concentrated to a final concentration of ∼200 μM using a Millipore 5000 MWCO filter operated under gas pressure. IAP was chosen for these studies based on the nature of the chemical bond formed upon the reaction of the cysteine sulfhydryl with the iodoacetamide group.[32,33] Spin-labeled construct purity and efficiency were verified through mass spectrometry mass analysis (University of Florida, Gainesville, FL).[33]

CW-EPR Spectra. CW-EPR spectra utilized for calculating the local tumbling volume have been reported previously, and details for data collection are given in the Supporting Information.[33] It is known that the ensemble of IDPs can be impacted by temperature as observed in CD spectroscopy;[66,67] as such, we performed control studies to evaluate how sensitive the EPR line shape of IA_3 was in terms of effects of temperature, TFE-induced viscosity, and denaturation by urea given in the Supporting Information (Figures S2−S4). Unless otherwise stated, all data have been collected at 27 °C because this was the easiest temperature for stability in our set up of ± 0.5 °C.[68] All samples are prepared with a final solution containing 2.5 mM sodium phosphate, 21.5 mM sodium chloride, and pH 7.0

Local Tumbling Volume X-Band EPR Data Analysis. From baseline-corrected area-normalized spectra, the local tumbling volume parameter (V_L) was calculated for continuous-wave (CW) X-band (∼9.5−9.8 GHz) EPR spectra in the fast limit (τ < 2 ns) according to eq 1, which gives the expression for V_L

$$V_L = \frac{kT\tau}{\eta} \tag{1}$$

where k is Boltzmann's constant, T is the absolute temperature, τ is the rotational correlation time, and η is the solvent viscosity.[69,70] Values of τ were determined from line shape simulations using the EWVoight program, which is based on Redfield theory and generously provided by Alex Smirnov (NCSU). All fits to the spectra are shown in Figures S5−7. The EWVoight program simulation provides values for the Lorentzian line widths of the three transitions that are subsequently used in eq 2

$$T_2(M)^{-1} = A + BM + CM^2 \tag{2}$$

where M is the nuclear spin quantum number of the M^{th} hyperfine line, $T_2(M)$ is the spin−spin relaxation time (which is inversely proportional to the homogeneous line width) of that line, and A, B, and C are the line shape parameters. In the fast motional regime, assumptions can be made and B and C alone can be used to determine rotational correlation time.[71−73] Values of τ were determined using eq 3

$$\tau = -1.22 \times 10^{-9} B(G) \tag{3}$$

where the value of B is obtained from solving eq 2 for the three hyperfine lines and is reported in Table S1.

Viscosity Measurements. The viscosity of the 0−40% (v/v) TFE solutions was determined using a Cannon-Fenske Viscometer (size 50) suspended in a water bath at 27.0 ± 0.3 °C and is reported in Supporting Information Tables S2,S3. The measurements were repeated four times for reproducibility. The solutions were prepared in 5% increments by combining the appropriate amount of TFE and the pH 7.4 buffer described previously.[33,36] The measurements were collected in units of seconds and converted to kinematic viscosity by using the conversion factor of the viscometer. The kinematic viscosity, which was expressed in units of centistokes (cS), was converted to dynamic viscosity (kg $m^{-1}s^{-1}$) using the densities of each of the solutions.

CW W-Band Electron Paramagnetic Resonance. CW W-band EPR spectra were collected on a Bruker Elexsys 680 spectrometer equipped with a W-band ENDOR resonator at the National High Magnetic Field Lab (NHMFL) in Tallahassee, FL. Temperature was regulated by the use of a CF935 Cyrostat (Oxford Instruments). Samples were prepared by concentrating samples studied at the X-band to approximately 2 mM spin-labeled protein. Samples were loaded into 0.15 i.d. × 0.25 o.d. suprasil quartz capillary tubes (Vitrocom, Mountain Lakes, NJ) and sealed with X-Sealant. The capillary tube with the sample was placed inside a quartz tube with a 0.50 i.d. × 0.90 o.d. that was sealed at one end. All experiments reported were performed at 27 ± 1 °C, unless otherwise stated. All spectra were collected as 180 Gauss (G) scans with a 0.0042 mW incident microwave power. The 100 kHz field modulation amplitude and time constant of the detector were optimized to provide the maximum signal-to-noise ratio with no line broadening. All spectra are reported as an average of ∼15 scans. Spectra are given in the Supporting Information (Figure S8)

Multifrequency CW X- and W-Band EPR Spectral Line Shapes Fitting. The EPR spectral line shapes of the CTD sites, Y57C, N58C, K59C, L60C, and K61C labeled with the IAP spin label at both X- and W-bands were simulated using the Labview program for fitting multicomponent CW-EPR spectra, written by Dr. Christian Altenbach from the laboratory of Dr. Wayne Hubbell at the University of California, Los Angeles. The experimental line shapes were normalized and phased before being loaded into the program. All of the EPR spectral line shapes could be fit with one component assuming isotropic motion. The g-tensor values for g_{xx}, g_{yy}, and g_{zz} were determined experimentally from the rigid limit spectrum of free IAP spin label at the W-band at 150 K and are 2.00821, 2.00641, and 2.00205; respectively.[35] The g-tensor values were held constant for each fit. The isotropic A-tensor (A1), the isotropic rotational diffusion tensor (Rbar), and the isotropic Lorentzian line width tensor (W1) were all allowed to vary. The definitions of the parameters were described by Budil et al.[74] Results from spectral fitting are given in Supporting

Information Tables S4-S5. Similar results were obtained for correlation times from multifrequency X-band and W-band fitting and those obtained using the Redfield fast-limit simulation (EWVoight) of X-band data.

ODNP Sample Preparation. The concentration of WT and spin-labeled IA_3 constructs was calculated by measuring the A_{214nm} value at diluted volumes of each stock solution in triplicate. The extinction coefficient, ε_{214nm}, for each construct was calculated as 140,794 $M^{-1}cm^{-1}$ (wildtype), 140,976 $M^{-1}cm^{-1}$ (V8P1), 140,985 $M^{-1}cm^{-1}$ (S9P1), 140,985 $M^{-1}cm^{-1}$ (S14P1), 140,883 $M^{-1}cm^{-1}$ (N58P1), and 140,978 $M^{-1}cm^{-1}$ (K59P1).[75] Spin-label concentration was verified using an IAP standard curve for S14P1 and was >90% comparable to A_{214nm} measured protein concentration. Due to comparable spin-label concentration and >95% spin labeling efficiency determined through mass spectrometry mass analysis, protein concentration was used for sample preparation and data analysis. X-band (9.5 GHz) CW-EPR absorption spectra for standard curve, spin count, and verification of sample integrity before and after ODNP were collected at room temperature using a Magnettech MiniScope MS-5000 benchtop or Bruker E500 spectrometer with a dielectric resonator. Spectra were reported as an average of 16 scans with 120 mT sweep width, 0.2 mT modulation amplitude, 100 kHz modulation frequency, and 1 mW incident microwave power (2 mW incident microwave power on Bruker E500). Each sample was prepared to ~150 μM protein concentration: 150 μL of autoclaved nH_2O, and 350 μL of protein in buffer (as described for CW-EPR sample preparation). This dilution factor was utilized to have the buffer ionic strength equivalent to those used during EPR and CD investigations with and without TFE addition.[32,33,36] Approximately 3.5 μL was drawn into 0.6 mm I.D. × 0.84 mm O.D. quartz capillary tubes via capillary action. The samples were sealed with a protective layer of Critoseal on the top and beeswax on the bottom (to protect samples from TFE evaporation).

ODNP Data Collection. Overhauser DNP was performed at a 0.35 T field using a Bruker EMX CW-EPR spectrometer, a Bruker Avance NMR console, a Bruker ER4119HS microwave resonator, and a custom-built 10 W 9.8 GHz microwave source system similar to the one described in 76. The NMR probe and sample were inserted into a ventilated quartz tube inside the resonator. Building air was flowed through the quartz tube for temperature control. All ODNP measurements were performed at room temperature with a deviation of ± 0.5 °C. The microwave resonator was tuned to ~9.8 GHz, the rf tuning circuit was tuned to ~14.8 MHz, and the magnetic field was set on resonance with the central electron spin transition. The ^{1}H free induction decay signal and the $T_{1,1H}$ relaxation time for each sample were measured as a function of microwave power from 0 to ~200 mW. Both the $T_{1,1H}$ and $T_{1,0}$ (spin lattice relaxation of the sample without spin label) were measured using inversion recovery pulse sequences. Each ODNP experiment was repeated three times. ODNP data and analysis are given in the Supporting Information (Figures S9 and S10, Tables S6 and S7) and follow the procedures of Han and co-workers.[55,57,77]

RESULTS AND DISCUSSION

***IA_3* Is a Bimodal Domain IDP.** The global sequence of IDPs can be evaluated in terms of their amino acid sequences, specifically focusing on hydropathy and fractional charge distribution of positive, f_+, and negative, f_-, amino acids.[1,2,4−6,17,20] The net fraction of charged residues of the global sequence is defined as FCR = $(f_+ + f_-)$. The global net charge per residue (NCPR) over the entire IDP sequence is defined as $|NCPR| = |f_+ - f_-|$.[5] Using the software localCIDER (http://pappulab.wustl.edu/CIDER),[4] these parameters can be readily calculated for amino acid sequences as a function of solution pH, thus allowing for fractional charges and distributions to include partial charges on histidine residues based on the standard pK_a values for amino acid side chains.

Five different conformationally based subclasses have been defined based on global sequence values of *FCR* and |*NCPR*|.[2,7] The graphical depiction of this "phase plot" has been termed a Das−Pappu plot (Figure 3A) with five regions, termed R1, R2, R3, and R4/R5 that differ in their *FCR* and |*NCPR*| parameters, and which have predicted characteristics of their structural ensembles.[4,5,17] More specifically, amino acid sequences with $FCR < 0.25$ and $NCPR < 0.25$ reside in region R1 adopt globule conformations. This region is sampled by weak polyampholytes/polyelectrolytes and polar tracks. Regions R4/R5 represent the other extreme for $FCR > 0.35$ and $NCPR > 0.35$ containing acid- versus base-rich polyelectrolytes, respectively. Because of the electrostatic repulsions between charged side chains, these sequences sample semiflexible worm-like conformations. Region 3, with $FCR > 0.35$ and $NCPR \leq 0.35$, is composed of strong polyampholytes that can form either coils or hairpins depending on the combination of *FCR* and their charge patterning. Thus, κ is a parameter that provides a quantitative measure of the distribution of charges within a given amino acid sequence.[2] It is very useful to describe different distribution patterns of charged amino acids in IDPs with identical amino acid compositions. As charges are segregated within the linear sequence, $\kappa \rightarrow 1$ (Figure 3B), hairpin conformations are favored. As charges are more interspersed, $\kappa \rightarrow 0$, stabilizing coil-like conformations. The mathematical calculation of κ has been described by Pappu and co-workers,[2] as further described below. The remaining phase space, R2 given by $0.25 \leq FCR \leq 0.35$ and $NCPR \leq 0.35$, is populated with sequences that adopt chimeras of globules and coils and are oftentimes those sequences that undergo binding-induced conformational changes to a structured state. Overall, the types of conformational ensembles of IDRs/IDPs have been shown to be dictated by low hydropathy and a combination of both κ and *FCR*.[1]

Analysis of the IA_3 sequence according to these methods shows that the two domains of IA_3 reside within different conformational subclasses in the Das−Pappu plot and differ in their hydropathy, *FCR*, |*NCPR*|, and κ parameters. The IA_3-NTD (1−32 a.a.; $FCR = 0.344$; $|NCPR| = 0.031$) falls within region R2: a globule to coil depending on the context, whereas the IA_3-CTD (33−68 a.a.; FCR = $\underline{0.417}$; $|NCPR| = 0$) is characterized by R3, a coil to hairpin conformation (Figure 3A). These values were calculated with CIDER for the *S. cerevisiae* IA_3 sequence (Figure 3C) at pH 7.0. Our expression construct contains a HIS_6 tag (`LEHHHHHH`), which when included in the calculation slightly modifies the values for the CTD as depicted in Figure 3A. However, it is unknown if the presence of the HIS tag modulates the conformational properties of IA_3. Figure 3D plots the sequence-dependent values of *NCPR* over a stretch of 5 amino acids ($NCPR_5$),[4] showing a differences in the range of $NCPR_5$ values between the two domains. Specifically, values for the NTD range between $-1 \leq NCPR_5 \leq 1$, whereas values range between $-3 \leq NCPR_5 \leq 2$ for the CTD. Additionally, the charge patterning

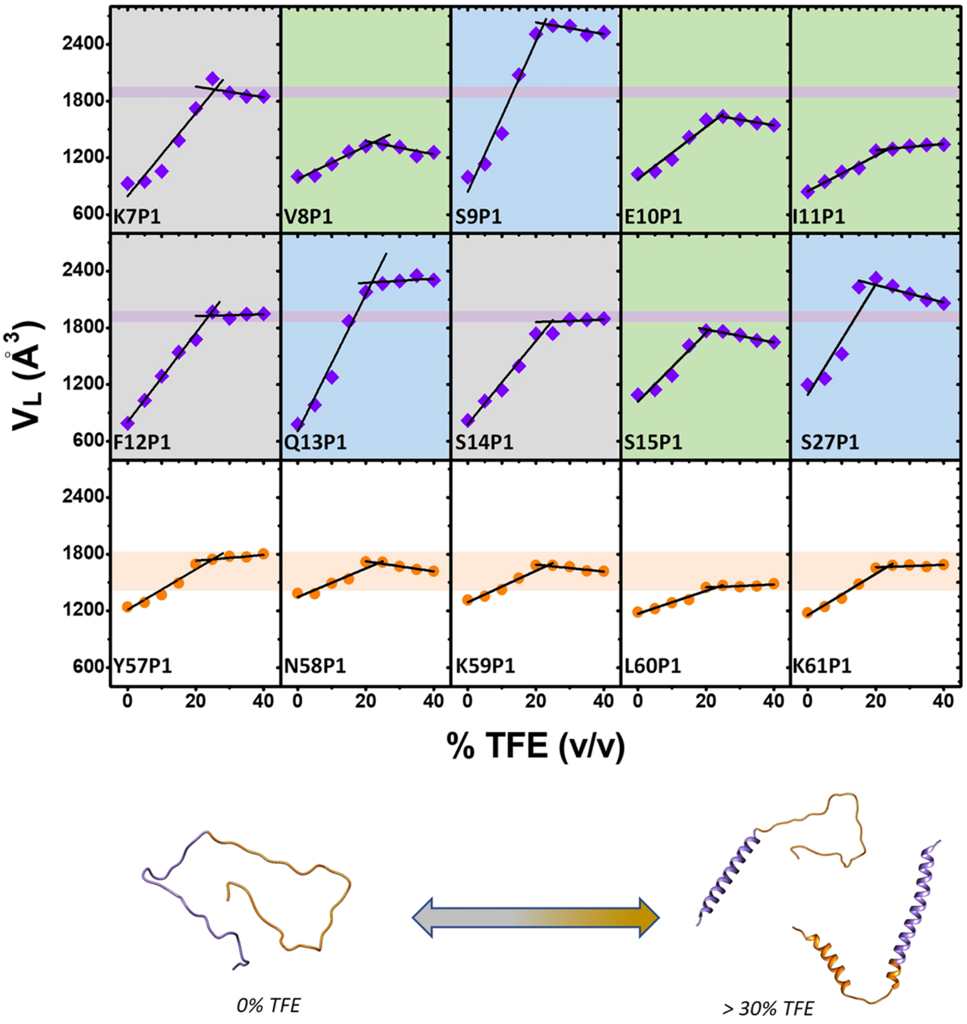

Figure 4. V_L analysis trends during TFE titration for NTD (purple squares) and CTD (orange circles) P1-IA$_3$ variants, where solid lines are fits to the two linear regions as discussed within the text. Horizontal purple bars represent the average V_L values for P1 constructs with WT helicity in the TFE-folded state, with background shading of gray = WT helical propensity, green < WT helical propensity, blue > WT helical propensity. The light orange bar shows the similar average V_L behavior for CTD residues, and all CTD construct studies here have overall total helicity similar to WT.[33] In all plots, the sizes of the data points are larger than the error in the measurements. Data were collected at 27 °C in triplicate for each sample.

of the *S. cerevisiae* IA$_3$ CTD is more segregated (i.e., $\kappa_{\mathrm{Cterm}}/\kappa_{\mathrm{Nterm}} \sim 3$) than its NTD sequence (Figure 3B).

The impact of these IDP conformation ensemble parameters on the two disparate domains of IA$_3$ has been seen in the crystallographic complex,[21] as well as in SDSL EPR spectroscopy,[32,33] NMR spectroscopy,[29] and fluorescence spectroscopy investigations of IA$_3$.[31] However, given that many of these earlier investigations were performed prior to the emerging knowledge of how sequence impacts IDP conformation, the results were not discussed in terms of the sequence parameters of IA$_3$. It is noteworthy that our biophysical experiments and IDP parameter analysis of IA$_3$ are performed at pH 7.0, NMR studies are performed at pH 5.5,[28] whereas the kinetic inhibition studies of YPRA by IA$_3$ are performed at pH 3–4.5,[27] likely reflective of the pH within the yeast vacuole. Future EPR and ODNP studies are planned to be performed on *S. cerevisiae*[36] as well as other yeast IA$_3$ constructs without a HIS-tag and as a function of pH and concentration.

Local Tumbling Volume Reflects Local IDP Compaction. The CW X-band EPR spectra of P1-labeled *S. cerevisiae* IA$_3$ have been published previously.[32−35] All CW X-band EPR spectra for IA$_3$ in solution are reflective of the motionally averaged regime, also referred to as the isotropic limit or fast limit (τ_c < 2 ns). These motionally narrowed spectral line shapes can be analyzed in terms of the local tumbling volume (V_L) parameter.[32,69,70] From eq 1, the value of V_L is directly proportional to the spin-label correlation time, τ_c. Using V_L allows for comparison across the TFE titration because it corrects for changes in solution viscosity induced by increasing TFE. Correlation times were determined from simulation/fitting of CW X-band spectra for NTD-labeled sites (Figures S5−S7, Table S1) and multifrequency CW X-band/W-band spectra for CTD-labeled sites utilizing two different methods and software packages (Figure S8, Tables S4 and S5). The correlation time obtained from simulation of X-band EPR spectra of nitroxide comprises motional averaging from the tumbling of the macromolecule, fluctuations of the peptide backbone, and internal rotational motions of the spin label itself.[78,79] Thus, V_L represents the volume of correlated motion that the nitroxide spin label samples.

Figure 4 plots values of V_L as a function of % (v/v) TFE for each P1 site (NTD data as squares; CTD as circles) during the

Table 1. Summary of the V_L Parameters for *S. cerevisiae* IA_3

	V_{Lave} (Å^3)			
	0%TFE	40% TFE	ΔV_{Lave} (Å^3)	$d\ V_{Lave}/d$%TFE (Å^3/%TFE)
NTD[a]	840 ± 130	1900 ± 40	1050 ± 50	30 ± 4
CTD	1260 ± 60	1600 ± 100	400 ± 100	11 ± 2

[a] For the NTD calculations, only those constructs with WT TFE-induced helicity were averaged.

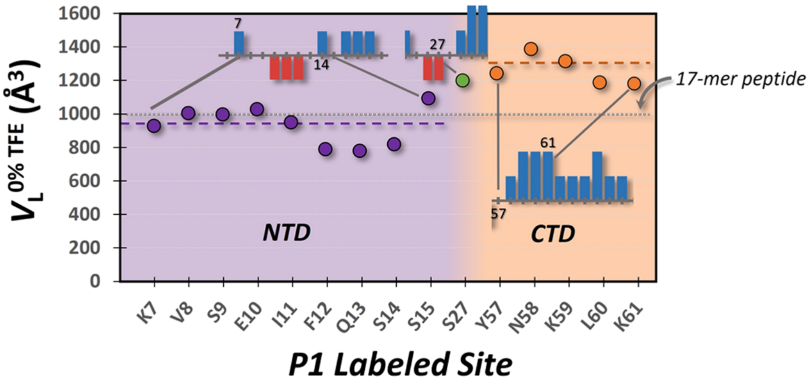

Figure 5. Graphical representation of V_L values for NTD (purple) and CTD (orange) P1-labeled sites of the intrinsically disordered state of IA_3. Dashed lines represent the V_L average values of each domain, with $V_{Lavg\ (NTD)}$ = 840 ± 40 Å^3 and $V_{Lavg\ (CTD)}$ = 1260 ± 90 Å^3. Data for S27 (green) were not included in either the NTD or CTD calculations and are defined here as a linker region based on the distribution of the $NCPR_5$ values (shown as insets). There is a statistically significantly smaller local tumbling volume of the NTD residues compared to the CTD. The dark gray dotted line at 1000 Å^3 represents a value obtained for a 17-mer alanine peptide.[69,70]

transition from disordered to α-helix. Values of V_L are lowest at 0% TFE and increase with the addition of TFE. Solid lines through the data points are linear fits to show that V_L increases linearly until the 20−25% TFE marks and then relatively levels off, with a slight up- or downslope attributable to errors in the simulation method utilized with the more anisotropic spectra.[70]

The observed trends in the dependence of V_L as a function of %(v/v) TFE can be understood by considering the three sources of flexibility that contribute to the motional averaging of the CW X-band nitroxide EPR line shape.[79] When disordered in solution, although the overall tumbling of the unstructured 7.6 kDa peptide may be > 1 ns, the backbone is likely undergoing large amplitude fluctuations, resulting in locally high mobility of the spin label with a small volume of space being sampled, i.e., the local tumbling volume is small due to the flexibility of the protein backbone. As the α-helix is formed with an increasing TFE percentage, the rigidity of the helix causes the backbone fluctuations to become smaller, and the spin label motion becomes less isotropic as it is restricted by the formation of the helix and hence the "volume" that it samples increases due to both the local modes of motion of the spin label and the larger volume occupied by the more rigid helix.[69,70] The relative leveling off of the local tumbling volume occurs because beyond 23% TFE, the protein is fully α-helical, and a higher percentage of TFE would not theoretically cause an increase to V_L.

The observed site-specific trends in values of V_L through the TFE-induced helical transition parallel three general trends that we reported earlier via $h_{(+1)}/h_{(0)}$ mobility parameter analysis of the EPR spectra.[32,33] First, results show more site-specific variation in the NTD compared to the CTD as a function of TFE show; second, the difference in V_L between 0 and 40% TFE (a.k.a. the degree of transition) is on average less for the CTD (ΔV_{Lavg} ~ 400 Å^3) than the NTD (ΔV_{Lavg} ~ 1000 Å^3); and third, the NTD undergoes a more cooperative TFE-induced transition than the CTD.

We previously discussed that the site-specific modulation in the EPR $h_{(+1)}/h_{(0)}$ mobility profiles as a function of %(v/v) TFE for NTD P1 sites tracks with changes with the TFE-induced helical propensity of the folded state upon P1 incorporation, as determined from CD analysis.[33] This means that as P1 is moved through the amphipathic helix of the NTD of IA_3 substitutions alter the TFE-induced helical propensity, where the greater the helical content at 30−50% TFE, the less mobile the EPR line shape. Consequently, a larger final value of V_L indicates a greater relative TFE-induced helical content of that variant. For example, the data for S9P1 in Figure 4 are representative of a P1 construct with > WT helical propensity and V8P1 represents a construct with < WT helical propensity. For comparisons made in this report, when discussing the two domains, we will utilize data from NTD sites with WT TFE-induced helicity (K7P1, F12P1, S14P1). The TFE-induced conformational states of the two domains of IA_3 have different average values of compaction, with $V_{Lavg\ NTD}$ ~ 1900 Å^3 > $V_{Lavg\ CTD}$ ~ 1700 Å^3. This result demonstrates the strength of spin labeling to interrogate site-specific behavior of the separate domains compared to CD, which averages over the entire protein sequence.

Millhauser et al. has shown that the degree of cooperativity of an unstructured to helical transition is reflected by the magnitude of the change in V_L as a function of temperature (a.k.a. the magnitude of the slope) for spin-labeled 16-mer and 17-mer peptides.[69,70] Hence, we can extend that analysis and conclude that the slope of our graphs reflects the relative cooperativity of the TFE-induced transition of IA_3. Slopes for the four CTD sites are similar in value, and they are less in magnitude than those for NTD sites with WT helical propensity (K7P1, F12P1, S14P1), indicating that the NTD undergoes a more cooperative folding in TFE (Table 1). These differences in the degree of cooperativity of the transition were

Table 2. Summary of the ODNP Results

	site	ξ	k_σ ($s^{-1}M^{-1}$)	k_ρ ($s^{-1}M^{-1}$)	k_{low} ($s^{-1}M^{-1}$)	τ_c (ps)
NTD	V8P1	0.153 ± 0.019	58 ± 2	380 ± 45	500 ± 75	130 ± 30
	S9P1	0.140 ± 0.008	56 ± 1	400 ± 20	530 ± 35	130 ± 13
	S14P1	0.145 ± 0.014	55 ± 5	380 ± 16	500 ± 30	126 ± 5
CTD	N58P1	0.47 ± 0.14	57 ± 3	120 ± 40	70 ± 60	16 ± 11
	K59P1	0.36 ± 0.11	55 ± 11	150 ± 40	130 ± 70	38 ± 20
bulk	TEMPO[a]	0.27	94	353	366	54.1
	IAP[b]	0.22 ± 0.01	71 ± 3	325 ± 12	376 ± 40	75 ± 3

[a] Data taken from refs 51,52,55. [b] Values determined as described in ref 52 Errors represent standard deviations from replicate experiments.

also seen via $h_{(+1)}/h_{(0)}$ mobility parameter analysis reported earlier, where data were fit with a sigmoidal curve and with the fwhm of the derivative of that curve reflecting the cooperativity of the transition.[32,33]

Another noticeable difference between V_L of the NTD and CTD is the ***initial value*** in the intrinsically disordered state. Figure 5 plots V_L values for P1-labeled amino acid locations in the disordered state (0% TFE), revealing a trend that $V_{\text{Lavg (CTD)}}$ (1260 ± 60 Å^3) > $V_{\text{Lavg (NTD)}}$ (840 ± 40 Å^3). These volumes were calculated from average correlation times of τ_c = 0.19 ± 0.02 and 0.27 ± 0.03 ns; respectively. To increase our confidence in the values of correlation times obtained from X-band data simulations, W-band EPR spectra were collected for all IA$_3$ CTD constructs (Spectra and analysis in Supporting Information Figures S8/Tables S6–7). These results imply that the disordered conformational ensemble over the Y57 to K61 IA$_3$-CTD sequence, which has a local high positive charge density, is more expanded than the K-7 to S15 IA$_3$-NTD. This finding suggests that the local tumbling volume may be reflective of local expansion/compaction dictated by a local charge density that influences the fluctuations and collapse or expansion of the protein backbone. Additional experiments are under way to further evaluate this hypothesis.

It is noteworthy that $V_{\text{Lavg (CTD)}}$ > $V_{\text{Lavg (NTD)}}$ in the disordered state even with the presence of the HIS-tag, which has been predicted to strongly increase overall compaction of IDPs.[17] The EPR results for the disordered state of IA$_3$ indicate *less compaction* of the CTD compared to the NTD, even in the presence of the C-terminal HIS$_6$-tag. Because of this, we are confident that the presence of the HIS$_6$-tag is not obfuscating the V_L trends observed with our data. Nevertheless, future investigations will be made on constructs not containing a HIS-tag.

Work by Millhauser et al. on spin-labeled 17-mer alanine peptides [Ac-A-E-A-A-A-K-E-A-C(MTSSL)-A-K-E-A-A-A-K-A-NH2; MTSSL is methanethiosulfonate spin label] gave local tumbling volumes of 1000 Å^3 when unstructured, which is larger than IA$_3$ $V_{\text{Lavg(NTD)}}$ ~ 840 Å^3 even though IA$_3$ is a 4.5× larger protein. We interpret the similarity in the size of the local tumbling volume to reflect a parameter of the compaction of the peptide backbone in the disordered ensembles. For further comparison, V_L = 500 Å^3 was obtained for spin-labeled glutathione.[69,70] The larger V_L values observed for the IA$_3$ CTD (~ 1300 Å^3) are consistent with a more extended/rod-like structure as predicted for R3 IDP conformational sequences[2] and sequences with higher overall net local charge.[17] Thus, the higher local tumbling volume represents less compaction at those local sites within the protein backbone in the disordered ensemble. These results may also suggest that those residues destined to become more helical are actually more compacted in the unfolded state, whereas those sites that are not as cooperatively ordered are more expanded in the disordered state. Further, the results demonstrate the capability of SDSL to provide information about the mobility/compaction of the microenvironment in IDPs.

It is important to note that the correlation times obtained for IA$_3$ in the TFE-induced helical state represent motional averaging dominated by the correlation times of the internal modes of motion of the spin label and do not directly reflect the global tumbling volume of cylindrical IA$_3$. Millhauser predicts V_L ~ 2000 Å^3 for a perfectly helical 17-mer peptide at 10 °C. For their 17-mer peptide, where helicity was induced by lowering the temperature, they obtained V_L ~ 1800 Å^3. For IA$_3$, the TFE-induced helical transition of the separate NTD and CTD are V_L ~ 1900 Å^3 (τ_c = 0.79 ± 0.02 ns for wildtype like constructs) and V_L ~ 1600 Å^3 (τ_c = 0.66 ± 0.02 ns), respectively. Our values for IA$_3$ (a 68-mer peptide with ~ 34 amino acids per domain) approach an average limiting value over both domains of V_L < 2000 Å^3, again, similar to values observed for a 17-mer peptide, indicating that the observed upper limit of V_L is likely constrained by the flexibility of the spin label utilized. It is also possible that IA$_3$ does not form a single helical coil in TFE.

Hydration Dynamics Is Influenced by Charge Distribution. Here, low-field ODNP was performed on 3 spin-labeled variants of IA$_3$ that resides within the NTD (V8P1, S9P1, and S14P1) and 2 spin-labeled variants within the CTD (N58P1 and K59P1). ODNP results reveal dramatic differences in the NTD and CTD surface hydration diffusivities (Table 1, Figure 2). In the unstructured state of IA$_3$ in solution, P1-N-terminal sites give *surface-like* hydration diffusivity, with ξ_{avg}=0.15 ± 0.03. On the other hand, the two C-terminal P1 sites have ξ values of 0.5 ± 0.2 (N58P1) and 0.4 ± 0.2 (K59P1), indicating *bulk-like* hydration diffusivity. The CTD ξ values are unusually large. In fact, they are greater than values for a spin label in solution (ξ_{bulk}=0.27[52]) and for sites on double-stranded DNA (ξ = 0.23–0.26[59]), which were described as anomalously high compared to protein surfaces. The origin of these differences is described below.

Regarding the NTD, we find that the water diffusivity within the 5–10 Å shell of P1 does not differ with amino acid substitutions that alter the TFE-induced helical propensity (V8P1 < WT, V9P1 > WT, S14P1 ≈ WT), and by extension, folded state local tumbling volume.[33] The helical propensity of the TFE-induced state of V8P1 is similar to or less than CTD constructs studied here (with similar local tumbling volume), yet the hydration dynamics of the unstructured state of V8P1 is similar to those of the other NTD P1 constructs and not the CTD sites (for which it has similar TFE-induced behavior). Thus, this suggests that the hydration dynamics in the NTD are encoded by a parameter of the unfolded ensemble and not

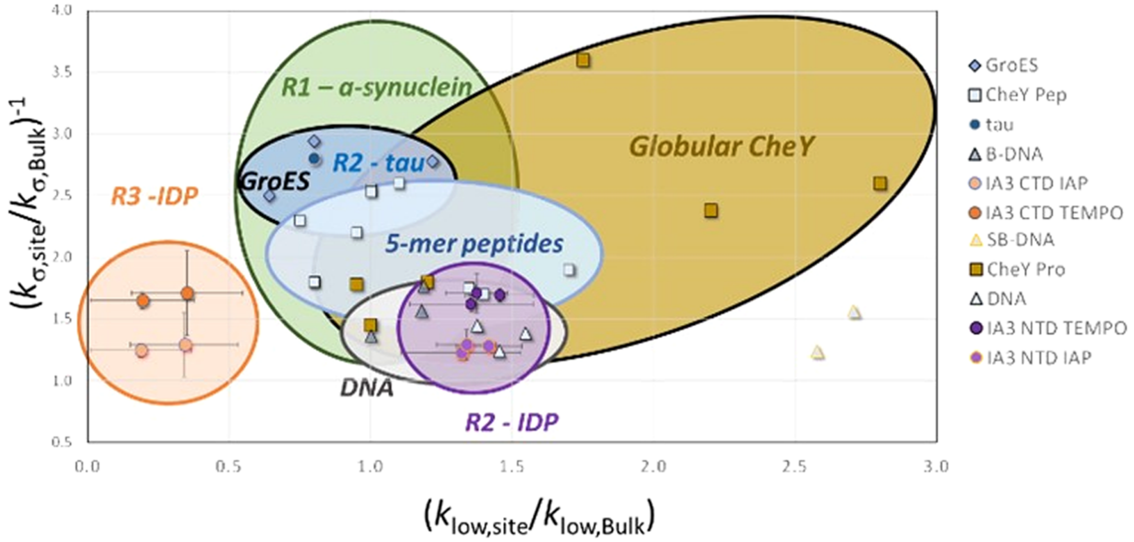

Figure 6. Scaled k_σ DW parameter as a function of scaled k_{low} for NTD (purple) and CTD (orange) IA$_3$-P1 constructs referenced to either TEMPO or IAP in bulk solution. Data for DNA;[59] GroES;[82] globular CheY, and 5-mer CheY peptides, tau and α−synuclein[57] taken from the respective literature references with scaling to TEMPO.[52]

sequence features that stabilize the folded state. V8P1 gives a good comparison to the CTD as it disrupts the TFE-induced helical transition and provides very similar local tumbling volumes to those seen for CTD sites. Yet, the hydration dynamics for V8P1 are nearly identical to those obtained for S9P1 and S19P1. Therefore, we interpret these results to suggest that it is not structure-inducing features that dictate hydration but rather the local charge density, NCPR$_5$, of the sequence that encodes for the hydration behavior.

The origin of the difference in ξ values of the two domains can be gleaned by separately evaluating k_σ and k_{low}, which represent different time scales of diffusing water as DW and BW, respectively.[55,57] Values of k_σ (Table 2) are relatively invariant ($k_{\sigma\mathrm{avg}}$ = 55 ± 2 $\mathrm{s}^{-1}\mathrm{M}^{-1}$) across P1-labeled constructs of both domains of IA$_3$. This finding indicates that picosecond DW dynamics within the 5−10 Å shell layer around the IA$_3$ surface are not impacted by amino acid sequence parameters such as κ or *NCPR*. In contrast, $k_{\mathrm{low,avg}}$ values are 510 ± 20 $\mathrm{s}^{-1}\mathrm{M}^{-1}$ for the NTD and 100 ± 40 $\mathrm{s}^{-1}\mathrm{M}^{-1}$ for the CTD, indicating that the slower bound water interactions differ leading to differences in ^{1}H−^{1}H relaxation.

By referencing to bulk water, $k_{\sigma,\,\mathrm{bulk}}$, a scaled parameter for DW can be calculated as in eq 4

$$k_{\sigma\mathrm{scaled}} = \left(\frac{k_{\sigma,\mathrm{site}}}{k_{\sigma,\mathrm{bulk}}}\right) \tag{4}$$

This value quantifies the marginal degree to which the surface diffusive water layer has been slowed compared to those waters interacting with TEMPO in water. We obtained an average $k_{\sigma\mathrm{scaled}}$ = 1.7 ± 0.04 over the narrow range of 1.6−1.7 for all 5 sites in IA$_3$. Comparison to the literature (Figure 6) reveals that DW of IA$_3$ is less hindered compared to DW of structured proteins, lipid bilayers, or membrane proteins, which have $k_{\sigma\mathrm{scaled}}$ values ranging up to > 6.[57,65,80] Interestingly, the DW behavior for both domains of IA$_3$ is similar, on average, to those previously seen for polyanionic DNA surfaces (1.4 ± 0.2-fold scaling).[59]

As described by Han and co-workers, the scaling "of DW dynamics can be viewed as reflecting on the enthalpic cost for disrupting and displacing the hydration water that is collectively strengthened by the attractive interactions between the protein surface and the hydrogen bonds of the local water network."[57] The narrow distribution of DW dynamics within and between the two domains of IA$_3$ indicates approximately equal enthalpic costs for displacing the local hydration water. The low scaling values indicate that these waters are more readily removed from the surface of IA$_3$ than most of those on structured proteins and the 5-mer peptide fragments of CheY.[57]

Previously, Han and co-workers characterized the DW dynamics in 5 amino acid peptide fragments of the protein CheY (with spin label in the center) and synthetic polyproline with lysine or aspartic acid (2−7 amino acids long with spin-labels on the N-termini) and found no correlation between the grand average hydropathy (GRAVY) values and DW dynamics. DW scaling for 5-mer CheY peptides and 5-mer to 10-mer polyproline peptides clustered between 1.6 and 2.7, marginally higher than what we observe for IA$_3$ (1.6−1.7).

Additionally, average $k_{\sigma\mathrm{scaled}}$ for IDPs α-synuclein[57,62,81] and Δtau-187[57,63,82] spread over values of 1.1 − 4.0 and cluster near 2.5, respectively. Han and co-workers concluded that variation in local charges on disordered 5-mer small peptides of the CheY surface does not modulate *DW* scaling (span values of 1.7 to 2.5). Here, with IA$_3$, we demonstrate that this conclusion holds true in larger IDP systems of up to ∼ 34 amino acids that span both R2 and R3 conformational space of a Pappu plot. The α-synuclein and Δtau-187 peptides in their study have sequences within the R1 and R2 Pappu phase space, respectively.

If values of k_σ for IA$_3$ do not vary across the two domains (i.e., as a function of *NCR* or κ), then the observed differences in NTD and CTD hydration diffusivity, ξ, must arise from alterations in the self-relaxation (k_ρ) of local waters, i.e., those that "tumble" or move with the protein surface. NTD sites have values of k_ρ ∼ 385 ± 10 $\mathrm{s}^{-1}\mathrm{M}^{-1}$, which are *slightly faster than* the self-relaxation rates obtained with TEMPO in water (353 $\mathrm{s}^{-1}\mathrm{M}^{-1}$).[52] In contrast, CTD P1 sites in IA$_3$ have k_ρ ∼ 140 ± 20 $\mathrm{s}^{-1}\mathrm{M}^{-1}$, which is a *slower rate than* that observed for waters solvating TEMPO in solution (Table 2). In efforts to understand the relatively low k_ρ values of the IA$_3$CTD P1 sites, we performed ODNP of the nitroxide IAP in buffer (Table 2). Scaling to IAP bulk values changed k_σ slightly, whereas k_ρ values of TEMPO and IAP were similar (Table 2); hence, we can conclude that these lowered k_{low} values do not arise from the IAP spin label and must then reflect properties of the amino acid sequence and structure that impact water relaxation.

We note that the errors reported here for k_ρ in Table 2 are all similar because the value of k_ρ, as given in eq 5

$$k_\rho = \frac{1}{C_{\text{SL}}}\left(\frac{1}{T_{1(0)}} - \frac{1}{T_{1,0}}\right) \tag{5}$$

is dependent on the inverse spin-labeled protein concentration, C_{SL} as well as differences in $T_{1(0)}$ and $T_{1,0}$, which represent the relaxation times obtained for a spin-labeled sample and non-spin-labeled sample, respectively. For IA$_3$CTD sites, the experimentally determined relaxation times for spin-labeled protein exhibited small changes in relaxation times compared to the non-spin-labeled sample (Table S7), leading to larger propagation of error in calculating values of k_ρ that originates from the error in the non-spin-labeled $T_{1,0}$ measurement. Although, according to Franck et al., greater certainty in $T_{1(0)}$ can be obtained by increasing protein concentrations, all values reported within were acquired for ~ 150 μM protein samples.[55]

For IA$_3$-NTD sites, k_{low} enhancements are approximately ~ 1.4 (defined as the ratio to k_{low} of TEMPO in water), which is similar to that obtained for the IDPs α-synuclein,[80,81] Δtau-187[63,82] and 5- residue peptides[57] studied by Han and co-workers (Figure 6). Both the number of bound water molecules and values of the local correlation time modulate k_{low} enhancements.[53] For correlation times > 1 ns, k_{low} enhancements > 1 are reflective of a population of bound water molecules.[57] Accordingly, this implies that the IA$_3$-NTD, which has k_{low} enhancements ~ 1.4, has a sparse to no BW population, if we assume that the unstructured ensemble of IA$_3$ (7.6 kD) has $\tau_{\text{rot}} > 1$ ns. Rotational correlation times of semirigid globular proteins can be predicted to be and have been shown to be > 2 ns for proteins as small as 3 kD.[83] Han and co-workers concluded that a marked difference in the hydration behavior of IDPs is the lack of BW harbored on the surface. This conclusion is based on assuming $\tau_{\text{rot}} > 1$ ns for α-synuclein and Δtau-187 proteins. The finding of similar ODNP results between IA$_3$-NTD and α-synuclein and Δtau-187 may not be surprising given that the sequence characteristics of these IDPs reside within subclasses R1 and R2. It is noteworthy that k_{low} enhancements for the 5-mer CheY peptides,[57] double-stranded DNA (12 bp and 24 bp),[59] and the folding chaperone GroES[82] are similar to those of the IA$_3$-NTD (Figure 6).

In contrast, for CTD sites of IA$_3$, we observe k_{low} with fractional enhancements, meaning that values of 0.2−0.3 were obtained. We currently cannot explain the molecular basis of these lowered enhancements. One possible explanation is that for IA$_3$, the assumption of $\tau_{\text{rot}} > 1$ ns may be incorrect. However, spectral simulation of CW X- and W-band nitroxide line shapes of individual spin-label spectra within the IA$_3$ NTD and CTD demonstrates that the coupled spin label and local backbone motion of IA$_3$CTD spin-labeled sites (a.a. 57−61) is *slower than* those observed over the NTD region (a.a. 7−15); in other words, CTD$\tau_c = 0.27 \pm 0.03$ ns > NTD $\tau_c = 0.19 \pm 0.02$ ns. Therefore, if we assume $\tau_{\text{rot}} > 1$ for the NTD, then it follows this would also be true for the CTD. Additionally, the local correlation times of P1 sites in IA$_3$ are all greater than those for TEMPO in water, suggesting that the enhancement values for k_{low} cannot be explained by the protein motion being faster than the small molecule or that the dynamics of the CTD are too fast for the ODNP analysis of k_{low}. Our observation that $k_{\text{low C-termini IA3}} < k_{\text{low TEMPO in water}}$ along with $k_{\sigma\text{ C-termini IA3}} \approx k_{\sigma\text{ N-termini IA3}} < k_{\sigma\text{ IAP}}$ is, to our knowledge, a unique finding in low-field ODNP studies of macromolecules.

Because k_{low} is obtained from the differences between the local electron−^{1}H cross-relaxation (k_σ) and local waters undergoing self-relaxation (k_ρ) as shown in eq 6

$$k_{low} = \frac{5}{3}k_\rho - \frac{7}{3}k_\sigma \tag{6}$$

k_{low} errors are also larger for CTD sites. Nevertheless, the data indicate ^{1}H−^{1}H self-relaxation within the CTD that is only 20−40% that of a spin label in water (Figure 6).

Although the origin of the lowered self-relaxation (k_ρ) of local waters of the CTD is currently unknown, it might be possible that "bound water" interacts differently in a highly charged local environment than with a nitroxide in water. Perhaps, the local electrostatic fields generated by the high local *NCPR* in the CTD (ranging between −3 to + 2) of IA$_3$ impact the slow-bound water relaxation properties differently than the bulk water−TEMPO interactions in solvent. Alternatively, the local dielectric constant may differ near the highly charged surface, which can impact the organization of water hydrogen bonds with charged side chains that overcome the possible hydrophobic contacts between water and the spin probe, leading to a lessened effect on water self-relaxation. Hence, we postulate that a reason for the different values of ξ in the two domains in IA$_3$ arises from the way the "slower bound water molecules" interact with the highly charged surface of the CTD of IA$_3$ and that sequence charge distribution may modulate this behavior and be a way to "encode" IDP conformational ensemble and function. Future studies are underway to test this concept on additional R3, R4, and R5 sequences.

■ ASSOCIATED CONTENT

Supporting Information

The Supporting Information is available free of charge at https://pubs.acs.org/doi/10.1021/acs.jpcb.3c06170.

IA$_3$ sequence alignments, helical wheel projections, figures showing side chain interactions in crystal complex, mass spectrometry results and summary of CD parameters discussed within the text (PDF)

Accession Codes

IA$_3$: P01094

■ AUTHOR INFORMATION

Corresponding Author

Gail E. Fanucci − *Department of Chemistry, University of Florida, Gainesville, Florida 32611, United States;* orcid.org/0000-0003-1960-160X; Email: fanucci@chem.ufl.edu

Authors

Katie M. Dunleavy − *Department of Chemistry, University of Florida, Gainesville, Florida 32611, United States*

Tianyan Li – *Department of Chemistry, University of Florida, Gainesville, Florida 32611, United States*
Eugene Milshteyn – *Department of Chemistry, University of Florida, Gainesville, Florida 32611, United States*
Afnan M. Jaufer – *Department of Chemistry, University of Florida, Gainesville, Florida 32611, United States*
Shamon A. Walker – *Materials Research Laboratory, University of California, Santa Barbara, California 93106, United States*

Complete contact information is available at:
https://pubs.acs.org/10.1021/acs.jpcb.3c06170

Author Contributions

K.M.D., E.M., and A.M.J. performed mutagenesis, protein expression, purification, and spin labeling of IA_3 for this work. K.M.D and S.W. performed and analyzed all low-field ODNP data. K.M.D. wrote the initial manuscript draft with E.M. E.M. performed CW-EPR experiments, viscosity measurements, and calculations of local tumbling volumes. T.L. performed all IA_3 sequence analyses. A.M.J. performed structural analysis, helped generate structural figures, calculated parameters related to tumbling volume changes, and proofread the final manuscript. K.M.D., A.M.J., and G.E.F. edited the final manuscript. All authors have read and approved of the manuscript.

Funding

This study was supported by NSF (MCB-1715384; MCB-1329467GEF) and NIH (S10 RR031603; GEF), and support for the ODNP studies was provided by the Deutsche Forschungsgemeinschaft (DFG, German Research Foundation) under Germany's Excellence Strategy—EXC-2033—Project number 39067787, and use of the Shared Experimental Facilities of the Materials Research Science and Engineering Center (MRSEC) at UC Santa Barbara (DMR 1720256) is gratefully acknowledged. The UC Santa Barbara MRSEC is a member of the NSF-supported Materials Research Facilities Network (www.mrfn.org). Part of this work was performed at the National High Magnetic Field Laboratory (NHMFL) (DMR−1157490 and DMR-2128556) and the State of Florida.

Notes

The authors declare no competing financial interest.

■ ACKNOWLEDGMENTS

The authors would like to thank Prof. Song-i Han, UCSB, for helpful discussions regarding data analysis and interpretation, Likai Song, Ph.D., NHMFL, and Natasha L. Pirman for aid in collecting W-band EPR data, and Prof. Alex Smirnov, NCSU, for access to EWVoight software.

■ ABBREVIATIONS

TFE, 2, 2, 2-trifluoroethanol; ODNP, Overhauser dynamic nuclear polarization; IDP, intrinsically disordered proteins; NMR, nuclear magnetic resonance; CD, circular dichroism spectroscopy; MD, molecular dynamic simulations; CW-EPR, continuous-wave electron paramagnetic resonance; WT, wild type; YPRA, yeast proteinase A inhibitor; DW, diffusive water; BW, bound water

■ REFERENCES

(1) Bianchi, G.; Longhi, S.; Grandori, R.; Brocca, S. Relevance of Electrostatic Charges in Compactness, Aggregation, and Phase Separation of Intrinsically Disordered Proteins. *Int. J. Mol. Sci.* **2020**, *21*, 6208.

(2) Das, R. K.; Pappu, R. V. Conformations of Intrinsically Disordered Proteins Are Influenced by Linear Sequence Distributions of Oppositely Charged Residues. *Proc. Natl. Acad. Sci. U.S.A.* **2013**, *110*, 13392−13397.

(3) Dyson, H. J.; Wright, P. E. Intrinsically Unstructured Proteins and Their Functions. *Nat. Rev. Mol. Cell Biol.* **2005**, *6*, 197−208.

(4) Holehouse, A. S.; Das, R. K.; Ahad, J. N.; Richardson, M. O.; Pappu, R. V. Cider: Resources to Analyze Sequence-Ensemble Relationships of Intrinsically Disordered Proteins. *Biophys. J.* **2017**, *112*, 16−21.

(5) Mao, A. H.; Crick, S. L.; Vitalis, A.; Chicoine, C. L.; Pappu, R. V. Net Charge Per Residue Modulates Conformational Ensembles of Intrinsically Disordered Proteins. *Proc. Natl. Acad. Sci. U.S.A.* **2010**, *107*, 8183−8188.

(6) Uversky, V. N.; Gillespie, J. R.; Fink, A. L. Why Are ″Natively Unfolded″ Proteins Unstructured under Physiologic Conditions? *Proteins* **2000**, *41*, 415−427.

(7) Das, R. K.; Ruff, K. M.; Pappu, R. V. Relating Sequence Encoded Information to Form and Function of Intrinsically Disordered Proteins. *Curr. Opin. Struct. Biol.* **2015**, *32*, 102−112.

(8) Dunker, A. K.; Lawson, J. D.; Brown, C. J.; Williams, R. M.; Romero, P.; Oh, J. S.; Oldfield, C. J.; Campen, A. M.; Ratliff, C. M.; Hipps, K. W.; Ausio, J.; Nissen, M. S.; Reeves, R.; Kang, C.; Kissinger, C. R.; Bailey, R. W.; Griswold, M. D.; Chiu, W.; Garner, E. C.; Obradovic, Z. Intrinsically Disordered Protein. *J. Mol. Graph. Model.* **2001**, *19*, 26−59.

(9) Tompa, P. Intrinsically Unstructured Proteins. *Trends Biochem. Sci.* **2002**, *27*, 527−533.

(10) Wright, P. E.; Dyson, H. J. Intrinsically Unstructured Proteins: Re-Assessing the Protein Structure-Function Paradigm. *J. Mol. Biol.* **1999**, *293*, 321−331.

(11) Dunker, A. K.; Oldfield, C. J.; Meng, J.; Romero, P.; Yang, J. Y.; Chen, J. W.; Vacic, V.; Obradovic, Z.; Uversky, V. N. The Unfoldomics Decade: An Update on Intrinsically Disordered Proteins. *BMC Genomics* **2008**, *9* (Suppl 2), S1.

(12) Tompa, P. Intrinsically Disordered Proteins: A 10-Year Recap. *Trends Biochem. Sci.* **2012**, *37*, 509−516.

(13) Karush, F. Heterogeneity of the Binding Sites of Bovine Serum Albumin. *J. Am. Chem. Soc.* **1950**, *72*, 2705−2713.

(14) Pancsa, R.; Tompa, P. Structural Disorder in Eukaryotes. *PLoS One* **2012**, *7*, No. e34687.

(15) Habchi, J.; Tompa, P.; Longhi, S.; Uversky, V. N. Introducing Protein Intrinsic Disorder. *Chem. Rev.* **2014**, *114*, 6561−6588.

(16) Vihinen, M.; Torkkila, E.; Riikonen, P. Accuracy of Protein Flexibility Predictions. *Proteins* **1994**, *19*, 141−149.

(17) Marsh, J. A.; Forman-Kay, J. D. Sequence Determinants of Compaction in Intrinsically Disordered Proteins. *Biophys. J.* **2010**, *98*, 2383−2390.

(18) Baul, U.; Chakraborty, D.; Mugnai, M. L.; Straub, J. E.; Thirumalai, D. Sequence Effects on Size, Shape, and Structural Heterogeneity in Intrinsically Disordered Proteins. *J. Phys. Chem. B* **2019**, *123*, 3462−3474.

(19) Brocca, S.; Grandori, R.; Longhi, S.; Uversky, V. Liquid-Liquid Phase Separation by Intrinsically Disordered Protein Regions of Viruses: Roles in Viral Life Cycle and Control of Virus-Host Interactions. *Int. J. Mol. Sci.* **2020**, *21*, 9045.

(20) Muller-Spath, S.; Soranno, A.; Hirschfeld, V.; Hofmann, H.; Ruegger, S.; Reymond, L.; Nettels, D.; Schuler, B. From the Cover: Charge Interactions Can Dominate the Dimensions of Intrinsically Disordered Proteins. *Proc. Natl. Acad. Sci. U.S.A.* **2010**, *107*, 14609−14614.

(21) Li, M.; Phylip, L. H.; Lees, W. E.; Winther, J. R.; Dunn, B. M.; Wlodawer, A.; Kay, J.; Gustchina, A. The Aspartic Proteinase from Saccharomyces Cerevisiae Folds Its Own Inhibitor into a Helix. *Nat. Struct.* **2000**, *7*, 113−117.

(22) Bauerova, V.; Pichova, I.; Hruskova-Heidingsfeldova, O. Fungal Gene-Encoded Peptidase Inhibitors. *Curr. Med. Chem.* **2013**, *20*, 3041−3048.

(23) Bobrovs, R.; Jaudzems, K.; Jirgensons, A. Exploiting Structural Dynamics to Design Open-Flap Inhibitors of Malarial Aspartic Proteases. *J. Med. Chem.* **2019**, *62*, 8931−8950.

(24) Dunn, B. M. Structure and Mechanism of the Pepsin-Like Family of Aspartic Peptidases. *Chem. Rev.* **2002**, *102*, 4431−4458.

(25) Padrón-García, J. A.; Alonso-Tarajano, M.; Alonso-Becerra, E.; Winterburn, T. J.; Ruiz, Y.; Kay, J.; Berry, C. Quantitative Structure Activity Relationship of IA_3-Like Peptides as Aspartic Proteinase Inhibitors. *Proteins* **2009**, *75*, 859−869.

(26) Winterburn, T. J.; Phylip, L. H.; Bur, D.; Wyatt, D. M.; Berry, C.; Kay, J. N-Terminal Extension of the Yeast IA_3 Aspartic Proteinase Inhibitor Relaxes the Strict Intrinsic Selectivity. *FEBS J.* **2007**, *274*, 3685−3694.

(27) Phylip, L. H.; Lees, W. E.; Brownsey, B. G.; Bur, D.; Dunn, B. M.; Winther, J. R.; Gustchina, A.; Li, M.; Copeland, T.; Wlodawer, A.; Kay, J. The Potency and Specificity of the Interaction between the IA_3 Inhibitor and Its Target Aspartic Proteinase from Saccharomyces Cerevisiae. *J. Biol. Chem.* **2001**, *276*, 2023−2030.

(28) Green, T. B.; Ganesh, O.; Perry, K.; Smith, L.; Phylip, L. H.; Logan, T. M.; Hagen, S. J.; Dunn, B. M.; Edison, A. S. IA_3, an Aspartic Proteinase Inhibitor from Saccharomyces Cerevisiae, Is Intrinsically Unstructured in Solution. *Biochemistry* **2004**, *43*, 4071−4081.

(29) Ganesh, O. K.; Green, T. B.; Edison, A. S.; Hagen, S. J. Characterizing the Residue Level Folding of the Intrinsically Unstructured IA_3. *Biochemistry* **2006**, *45*, 13585−13596.

(30) Green, T.; Perry, K.; Smith, L.; Phylip, L. H.; Logan, T. M.; Hagen, S. J.; Dunn, B. M.; Edison, A. IA_3, a Yeast Proteinase a Inhibitor, Is Intrinsically Unstructured in Solution. *Sci. World J.* **2002**, *2*, 99−101.

(31) Narayanan, R.; Ganesh, O. K.; Edison, A. S.; Hagen, S. J. Kinetics of Folding and Binding of an Intrinsically Disordered Protein: The Inhibitor of Yeast Aspartic Proteinase Ypra. *J. Am. Chem. Soc.* **2008**, *130*, 11477−11485.

(32) Pirman, N. L.; Milshteyn, E.; Galiano, L.; Hewlett, J. C.; Fanucci, G. E. Characterization of the Disordered-to-A-Helical Transition of IA_3 by SDSL-EPR Spectroscopy. *Protein Sci.* **2011**, *20*, 150−159.

(33) Dunleavy, K. M.; Milshteyn, E.; Sorrentino, Z.; Pirman, N. L.; Liu, Z.; Chandler, M. B.; D'Amore, P. W.; Fanucci, G. E. Spin-Label Scanning Reveals Conformational Sensitivity of the Bound Helical Interfaces of IA_3. *Aims Biophys.* **2018**, *5*, 166−181.

(34) Casey, T. M.; Liu, Z. L.; Esquiaqui, J. M.; Pirman, N. L.; Milshteyn, E.; Fanucci, G. E. Continuous Wave W- and D-Band Epr Spectroscopy Offer "Sweet-Spots" for Characterizing Conformational Changes and Dynamics in Intrinsically Disordered Proteins. *Biochem. Biophys. Res. Com.* **2014**, *450*, 723−728.

(35) Song, L. K.; Liu, Z. L.; Kaur, P.; Esquiaqui, J. M.; Hunter, R. I.; Hill, S.; Smith, G. M.; Fanucci, G. E. Toward Increased Concentration Sensitivity for Continuous Wave Epr Investigations of Spin-Labeled Biological Macromolecules at High Fields. *J. Magn. Reson.* **2016**, *265*, 188−196.

(36) Dunleavy, K. M.; Oi, C.; Li, T.; Secunda, A.; Jaufer, A. M.; Zhu, Y.; Friedman, L.; Kim, A.; Fanucci, G. E. Hydrogen Bonding Compensation on the Convex Solvent-Exposed Helical Face of Ia(3), an Intrinsically Disordered Protein. *Biochemistry* **2023**, *62*, 1716−1724.

(37) Lehner, J.; Stoll, S. Modeling of Motional Epr Spectra Using Hindered Brownian Rotational Diffusion and the Stochastic Liouville Equation. *J. Chem. Phys.* **2020**, *152*, No. 094103.

(38) Martin, P. D.; Svensson, B.; Thomas, D. D.; Stoll, S. Trajectory-Based Simulation of Epr Spectra: Models of Rotational Motion for Spin Labels on Proteins. *J. Phys. Chem. B.* **2019**, *123*, 10131−10141.

(39) Tessmer, M. H.; Canarie, E. R.; Stoll, S. Comparative Evaluation of Spin-Label Modeling Methods for Protein Structural Studies. *Biophys. J.* **2022**, *121*, 3508−3519.

(40) Altenbach, C.; Lopez, C. J.; Hideg, K.; Hubbell, W. L. Exploring Structure, Dynamics, and Topology of Nitroxide Spin-Labeled Proteins Using Continuous-Wave Electron Paramagnetic Resonance Spectroscopy. *Methods Enzymol.* **2015**, *564*, 59−100.

(41) Torricella, F.; Pierro, A.; Mileo, E.; Belle, V.; Bonucci, A. Nitroxide Spin Labels and Epr Spectroscopy: A Powerful Association for Protein Dynamics Studies. *Biochim. Biophys. Acta, Proteins Proteomics* **2021**, *1869*, No. 140653.

(42) Sahu, I. D.; Lorigan, G. A. Site-Directed Spin Labeling Epr for Studying Membrane Proteins. *Biomed. Res. Int.* **2018**, *2018*, No. 3248289.

(43) Fanucci, G. E.; Cafiso, D. S. Recent Advances and Applications of Site-Directed Spin Labeling. *Curr. Opin. Struct. Biol.* **2006**, *16*, 644−653.

(44) Bonucci, A.; Palomino-Schatzlein, M.; Malo de Molina, P.; Arbe, A.; Pierattelli, R.; Rizzuti, B.; Iovanna, J. L.; Neira, J. L. Crowding Effects on the Structure and Dynamics of the Intrinsically Disordered Nuclear Chromatin Protein Nupr1. *Front. Mol. Biosci.* **2021**, *8*, No. 684622.

(45) Bonucci, A.; Murrali, M. G.; Banci, L.; Pierattelli, R. A Combined NMR and EPR Investigation on the Effect of the Disordered Rgg Regions in the Structure and the Activity of the RRM Domain of Fus. *Sci. Rep.* **2020**, *10*, No. 20956.

(46) Longhi, S.; Belle, V.; Fournel, A.; Guigliarelli, B.; Carriere, F. Probing Structural Transitions in Both Structured and Disordered Proteins Using Site-Directed Spin-Labeling Epr Spectroscopy. *J. Pept. Sci.* **2011**, *17*, 315−328.

(47) Kavalenka, A.; Urbancic, I.; Belle, V.; Rouger, S.; Costanzo, S.; Kure, S.; Fournel, A.; Longhi, S.; Guigliarelli, B.; Strancar, J. Conformational Analysis of the Partially Disordered Measles Virus N(Tail)-Xd Complex by SDSL EPR Spectroscopy. *Biophys. J.* **2010**, *98*, 1055−1064.

(48) Le Breton, N.; Longhi, S.; Rockenbauer, A.; Guigliarelli, B.; Marque, S. R. A.; Belle, V.; Martinho, M. Probing the Dynamic Properties of Two Sites Simultaneously in a Protein-Protein Interaction Process: A SDSL-EPR Study. *Phys. Chem. Chem. Phys.* **2019**, *21*, 22584−22588.

(49) Mileo, E.; Etienne, E.; Martinho, M.; Lebrun, R.; Roubaud, V.; Tordo, P.; Gontero, B.; Guigliarelli, B.; Marque, S. R.; Belle, V. Enlarging the Panoply of Site-Directed Spin Labeling Electron Paramagnetic Resonance (SDSL-EPR): Sensitive and Selective Spin-Labeling of Tyrosine Using an Isoindoline-Based Nitroxide. *Bioconjugate Chem.* **2013**, *24*, 1110−1117.

(50) Pirman, N. L.; Milshteyn, E.; Galiano, L.; Hewlett, J. C.; Fanucci, G. E. Characterization of the Disordered-to-Alpha-Helical Transition of IA_3 by SDSL-EPR Spectroscopy. *Protein Sci.* **2011**, *20*, 150−159.

(51) Franck, J. M.; Sokolovski, M.; Kessler, N.; Matalon, E.; Gordon-Grossman, M.; Han, S. I.; Goldfarb, D.; Horovitz, A. Probing Water Density and Dynamics in the Chaperonin Groel Cavity. *J. Am. Chem. Soc.* **2014**, *136*, 9396−9403.

(52) Franck, J. M.; Pavlova, A.; Scott, J. A.; Han, S. Quantitative Cw Overhauser Effect Dynamic Nuclear Polarization for the Analysis of Local Water Dynamics. *Prog. Nucl. Magn. Reson. Spectrosc.* **2013**, *74*, 33−56.

(53) Ortony, J. H.; Cheng, C.-Y.; Franck, J. M.; Kausik, R.; Pavlova, A.; Hunt, J.; Han, S. Probing the Hydration Water Diffusion of Macromolecular Surfaces and Interfaces. *New J. Phys.* **2011**, *13*, No. 015006.

(54) Kaminker, I.; Barnes, R.; Han, S. Overhauser Dynamic Nuclear Polarization Studies on Local Water Dynamics. *Methods Enzymol.* **2015**, *564*, 457−483.

(55) Franck, J. M.; Han, S. Overhauser Dynamic Nuclear Polarization for the Study of Hydration Dynamics, Explained. *Methods Enzymol.* **2019**, *615*, 131−175.

(56) McCarney, E. R.; Armstrong, B. D.; Kausik, R.; Han, S. Dynamic Nuclear Polarization Enhanced Nuclear Magnetic Resonance and Electron Spin Resonance Studies of Hydration and Local

Water Dynamics in Micelle and Vesicle Assemblies. *Langmuir* **2008**, *24*, 10062−10072.

(57) Barnes, R.; Sun, S.; Fichou, Y.; Dahlquist, F. W.; Heyden, M.; Han, S. Spatially Heterogeneous Surface Water Diffusivity around Structured Protein Surfaces at Equilibrium. *J. Am. Chem. Soc.* **2017**, *139*, 17890−17901.

(58) Hwang, L. L.-P.; Freed, J. H. J. Dynamic Effects of Pair Correlation Functions on Spin Relaxation by Translational Diffusion in Liquids. *J. Chem. Phys.* **1975**, *63*, 4017−4025.

(59) Franck, J. M.; Ding, Y.; Stone, K.; Qin, P. Z.; Han, S. Anomalously Rapid Hydration Water Diffusion Dynamics near DNA Surfaces. *J. Am. Chem. Soc.* **2015**, *137*, 12013−12023.

(60) Kausik, R.; Srivastava, A.; Korevaar, P. A.; Stucky, G.; Waite, J. H.; Han, S. Local Water Dynamics in Coacervated Polyelectrolytes Monitored through Dynamic Nuclear Polarization-Enhanced H NMR. *Macromolecules* **2009**, *42*, 7404−7412.

(61) Kausik, R.; Han, S. Dynamics and State of Lipid Bilayer-Internal Water Unraveled with Solution State 1h Dynamic Nuclear Polarization. *Phys. Chem. Chem. Phys.* **2011**, *13*, 7732−7746.

(62) Cheng, C. Y.; Wang, J. Y.; Kausik, R.; Lee, K. Y.; Han, S. An Ultrasensitive Tool Exploiting Hydration Dynamics to Decipher Weak Lipid Membrane-Polymer Interactions. *J. Magn. Reson.* **2012**, *215*, 115−119.

(63) Pavlova, A.; McCarney, E. R.; Peterson, D. W.; Dahlquist, F. W.; Lew, J.; Han, S. Site-Specific Dynamic Nuclear Polarization of Hydration Water as a Generally Applicable Approach to Monitor Protein Aggregation. *Phys. Chem. Chem. Phys.* **2009**, *11*, 6553−6554.

(64) Armstrong, B. D.; Choi, J.; Lopez, C.; Wesener, D. A.; Hubbell, W.; Cavagnero, S.; Han, S. Site-Specific Hydration Dynamics in the Nonpolar Core of a Molten Globule by Dynamic Nuclear Polarization of Water. *J. Am. Chem. Soc.* **2011**, *133*, 5987−5995.

(65) Hong, Y.; Najafi, S.; Casey, T.; Shea, J. E.; Han, S. I.; Hwang, D. S. Hydrophobicity of Arginine Leads to Reentrant Liquid-Liquid Phase Separation Behaviors of Arginine-Rich Proteins. *Nat. Commun.* **2022**, *13*, No. 7326.

(66) Jephthah, S.; Staby, L.; Kragelund, B. B.; Skepo, M. Temperature Dependence of Intrinsically Disordered Proteins in Simulations: What Are We Missing? *J. Chem. Theory. Comput.* **2019**, *15*, 2672−2683.

(67) Kjaergaard, M.; Norholm, A. B.; Hendus-Altenburger, R.; Pedersen, S. F.; Poulsen, F. M.; Kragelund, B. B. Temperature-Dependent Structural Changes in Intrinsically Disordered Proteins: Formation of Alpha-Helices or Loss of Polyproline II? *Protein Sci.* **2010**, *19*, 1555−1564.

(68) Frederick, T. E.; Goff, P. C.; Mair, C. E.; Farver, R. S.; Long, J. R.; Fanucci, G. E. Effects of the Endosomal Lipid Bis-(Monoacylglycero)Phosphate on the Thermotropic Properties of Dppc: A 2H NMR and Spin Label EPR Study. *Chem. Phys. Lipids* **2010**, *163*, 703−711.

(69) Miick, S. M.; Todd, A. P.; Millhauser, G. L. Position-Dependent Local Motions in Spin-Labeled Analogs of a Short Alpha-Helical Peptide Determined by Electron-Spin-Resonance. *Biochemistry* **1991**, *30*, 9498−9503.

(70) Todd, A. P.; Millhauser, G. L. Esr-Spectra Reflect Local and Global Mobility in a Short Spin-Labeled Peptide Throughout the Alpha-Helix-]Coil Transition. *Biochemistry* **1991**, *30*, 5515−5523.

(71) Marsh, D. *Experimental Methods in Spin-Label Spectral Analysis*; Plenum Press: New York and London, 1989.

(72) *Spin Labeling: Theory and Applications*; Academic Press: New York, 1976.

(73) Smirnova, T. I.; Smirnov, A. I. High-Field Esr Spectroscopy in Membrane and Protein Biophysics. In *EPR Spectroscopy in Membrane Biophysics*; Hemminga, M. A.; Berliner, L. J., Eds.; Springer: New York, 2007; Vol. *27*.

(74) Budil, D. E.; Lee, S.; Saxena, S.; Freed, J. H. Nonlinear-Least-Squares Analysis of Slow-Motion Epr Spectra in One and Two Dimensions Using a Modified Levenberg-Marquardt Algorithm. *J. Magn. Reson., Ser. A* **1996**, *120*, 155−189.

(75) Kuipers, B. J. H.; Gruppen, H. Prediction of Molar Extinction Coefficients of Proteins and Peptides Using Uv Absorption of the Constituent Amino Acids at 214 Nm to Enable Quantitative Reverse Phase High-Performance Liquid Chromatography−Mass Spectrometry Analysis. *J. Agric. Food Chem.* **2007**, *55*, 5445−5451.

(76) Armstrong, B. D.; Lingwood, M.; McCarney, E.; Brown, E. R.; Blümler, P.; Han, S. Portable X-Band System for Solution State Dynamic Nuclear Polarization. *J. Magn. Reson.* **2008**, *191*, 273−281.

(77) Moon, H.; Collanton, R. P.; Monroe, J. I.; Casey, T. M.; Shell, M. S.; Han, S.; Scott, S. L. Evidence for Entropically Controlled Interfacial Hydration in Mesoporous Organosilicas. *J. Am. Chem. Soc.* **2022**, *144*, 1766−1777.

(78) Hubbell, W. L.; Cafiso, D. S.; Altenbach, C. Identifying Conformational Changes with Site-Directed Spin Labeling. *Nat. Struct. Biol.* **2000**, *7*, 735−739.

(79) McHaourab, H. S.; Lietzow, M. A.; Hideg, K.; Hubbell, W. L. Motion of Spin-Labeled Side Chains in T4 Lysozyme. Correlation with Protein Structure and Dynamics. *Biochemistry* **1996**, *35*, 7692−7704.

(80) Fisette, O.; Paslack, C.; Barnes, R.; Isas, J. M.; Langen, R.; Heyden, M.; Han, S.; Schafer, L. V. Hydration Dynamics of a Peripheral Membrane Protein. *J. Am. Chem. Soc.* **2016**, *138*, 11526−11535.

(81) Cheng, C. Y.; Varkey, J.; Ambroso, M. R.; Langen, R.; Han, S. Hydration Dynamics as an Intrinsic Ruler for Refining Protein Structure at Lipid Membrane Interfaces. *Proc. Natl. Acad. Sci. U.S.A.* **2013**, *110*, 16838−16843.

(82) Pavlova, A.; Cheng, C. Y.; Kinnebrew, M.; Lew, J.; Dahlquist, F. W.; Han, S. Protein Structural and Surface Water Rearrangement Constitute Major Events in the Earliest Aggregation Stages of Tau. *Proc. Natl. Acad. Sci. U.S.A.* **2016**, *113*, E127−36.

(83) García de la Torre, J.; Huertas, M. L.; Carrasco, B. HydroNMR: Prediction of NMR Relaxation of Globular Proteins from Atomic-Level Structures and Hydrodynamic Calculations. *J. Magn. Reson.* **2000**, *147*, 138−146.